

## THE IMPACT OF GAS BULK ROTATION ON THE LYMAN $\alpha$ LINE

JUAN N. GARAVITO-CAMARGO, JAIME E. FORERO-ROMERO

Departamento de Física, Universidad de los Andes, Cra. 1 No. 18A-10, Edificio Ip, Bogotá, Colombia

AND

MARK DIJKSTRA

Institute of Theoretical Astrophysics, University of Oslo, Postboks 1029, 0858 Oslo, Norway

*Submitted for publication in ApJ*

### ABSTRACT

We present results of radiative transfer calculations to measure the impact of gas bulk rotation on the morphology of the Lyman  $\alpha$  emission line in distant galaxies. We model a galaxy as a sphere with an homogeneous mixture of dust and hydrogen at a constant temperature. These spheres have a solid-body rotation with maximum velocities in the range  $0 - 300 \text{ km s}^{-1}$  and neutral hydrogen optical depths in the range  $\tau_{\text{H}} = 10^5 - 10^7$ . We consider cases of a single central Lyman  $\alpha$  source, and a uniform distribution of sources. Our main result is that rotation introduces a dependence of the line morphology with viewing angle. Observations parallel to the rotation axis yield lines similar to the static case. The greatest difference is observed perpendicular to the rotation axis where the intensity at the line center increases with rotational velocity. For homogeneously distributed sources the line becomes single peaked at rotational velocities larger than half the line width in the static case. However, rotation does not induce any significant anisotropy in the total line intensity or in the escape fraction.

*Subject headings:* galaxies: high-redshift — line: formation — methods: numerical — radiative transfer

### 1. INTRODUCTION

The detection of strong Ly $\alpha$  emission lines has become an essential method in extra-galactic astronomy to find distant star-forming galaxies (Partridge & Peebles 1967; Rhoads et al. 2000; Gawiser et al. 2007; Koehler et al. 2007; Ouchi et al. 2008; Yamada et al. 2012; Schenker et al. 2012; Finkelstein et al. 2013). The galaxies detected using this method receive the name of Ly $\alpha$  emitters (LAEs). A detailed examination of this galaxy population has diverse implications for galaxy formation, reionization and the large scale structure of the Universe. Attempts to fully exploit the physical information included in the Ly $\alpha$  line require an understanding of all the physical factors involved in shaping the line. Due to the resonant nature of this line, these physical factors notably include temperature, density and bulk velocity field of the neutral Hydrogen in the emitting galaxy and its surroundings.

A basic understanding of the quantitative behavior of the Ly $\alpha$  line has been reached through analytic studies in the case of a static configurations, such as uniform slabs (Adams 1972; Harrington 1973; Neufeld 1990) and uniform spheres (Dijkstra et al. 2006). Analytic studies of configurations including some kind of bulk flow only include the case of a sphere with a Hubble like expansion flow (Loeb & Rybicki 1999).

A quantitative description of the Ly $\alpha$  line has been reached through Monte Carlo simulations (Auer 1968; Avery & House 1968; Adams 1972). In the last two decades these studies have become popular due to the availability of computing power. Early into the 21st century, the first studies focused on homogeneous and static

media (Ahn et al. 2000, 2001; Zheng & Miralda-Escudé 2002). Later on, the effects of clumpy media (Hansen & Oh 2006) and expanding/contracting shell/spherical geometries started to be studied (Verhamme et al. 2006; Dijkstra et al. 2006; Ahn et al. 2014). Similar codes have applied these results to semi-analytic models of galaxy formation (Orsi et al. 2012; Garel et al. 2012) and results of large hydrodynamic simulations (Forero-Romero et al. 2011, 2012; Behrens & Niemeyer 2013). Recently, Monte Carlo codes have also been applied to the results of high resolution hydrodynamic simulations of individual galaxies (Laursen et al. 2009; Barnes et al. 2011; Verhamme et al. 2012; Yajima et al. 2012). Meanwhile, recent developments have been focused on the systematic study of clumpy outflows (Dijkstra & Kramer 2012) and anisotropic velocity configurations (Zheng & Wallace 2013).

The recent studies of galaxies in hydrodynamic simulations (Laursen et al. 2009; Barnes et al. 2011; Verhamme et al. 2012; Yajima et al. 2012) have all shown systematic variations in the Ly $\alpha$  line with the viewing angle. These variations are a complex superposition of anisotropic density configurations (i.e. edge-on vs. face-on view of a galaxy), the inflows observed by gas cooling and the outflows included in the supernova feedback process of the simulation. These bulk flows physically correspond to the circumgalactic and intergalactic medium (CGM and IGM). These effects are starting to be studied in simplified configurations that vary the density and wind characteristics (Zheng & Wallace 2013; Behrens et al. 2014).

However, in all these efforts the effect of rotation, which is an ubiquitous feature in galaxies, has not been systematically studied. The processing of the Ly $\alpha$  photons in a rotating interstellar medium (ISM) must have

some kind of impact in the Ly $\alpha$  line morphology.

Performing that study is the main goal of this paper. We investigate for the first time the impact of rotation on the morphology of the Ly $\alpha$  line. We focus on a simplified system: a spherical gas cloud with homogeneous density and solid body rotation, to study the line morphology and the escape fraction in the presence of dust. We base our work on two independent Monte Carlo based radiative transfer codes presented in Forero-Romero et al. (2011) and Dijkstra & Kramer (2012).

This paper is structured as follows: In §2 we present the implementation of bulk rotation into the Monte Carlo codes, paying special attention to coordinate definitions. We also present a short review of how the Ly $\alpha$  radiative transfer codes work and list the different physical parameters in the simulated grid of models. In §3 we present the results of the simulations, with special detail to quantities that show a clear evolution as a function of the sphere rotational velocity. In §4 we discuss the implications of our results in the interpretation of LAEs observations with high resolution spectroscopy. In the last section we present our conclusions.

In this paper we express a photon's frequency in terms of the dimensionless variable  $x \equiv (\nu - \nu_a)/\Delta\nu_\alpha$ , where  $\nu_\alpha = 2.46 \times 10^{15}$  Hz is the Ly $\alpha$  resonance frequency,  $\Delta\nu_\alpha \equiv \nu_\alpha \sqrt{2kT/m_p c^2} \equiv \nu_a v_{\text{th}}/c$  is the Doppler broadening of the line which depends on the neutral gas temperature  $T$  scattering the radiation or equivalently the thermal velocity  $v_{\text{th}}$  of the atoms. For the temperature  $T = 10^4$  K used in our radiative transfer calculations the thermal velocity is  $v_{\text{th}} = 12.8 \text{ km s}^{-1}$ .

## 2. MODELS OF BULK GAS ROTATION

Describing the kinematics of gas rotation in all generality is a complex task, specially at high redshift where there is still missing a thorough observational account of rotation in galaxies beyond  $z > 1.0$ . Even at low redshifts there is a great variation in the shape of the rotation curve as observed in HI emission as a function of the distance to the galaxy center. However there are two recurrent features. First, in the central galactic region the velocity increases proportional to the radius, following a solid rotation behavior. Second, beyond a certain radius the rotation curve tends to flatten. An ab-initio description of such realistic rotation curves in simulations depends on having access to the dynamic evolution of all mass components in the galaxy: stars, gas and dark matter. Such level of realism is extremely complex to achieve, specially if one wants to get a systematic description based on statistics of simulated objects.

Following the tradition of studies of Ly $\alpha$  emitting systems, we implement a model with simplified geometry. We assume that the gas is homogeneously distributed in a sphere that rotates as a solid body with constant angular velocity. This simple model will contain only one free parameter: the linear velocity at the sphere's surface,  $V_{\text{max}}$ .

### 2.1. Detailed Implementation of Rotation

In the Monte Carlo code we define a Cartesian coordinate system to describe the position of each photon. The origin of this system coincides with the center of the sphere and the rotation axis is defined to be  $z$ -axis. With

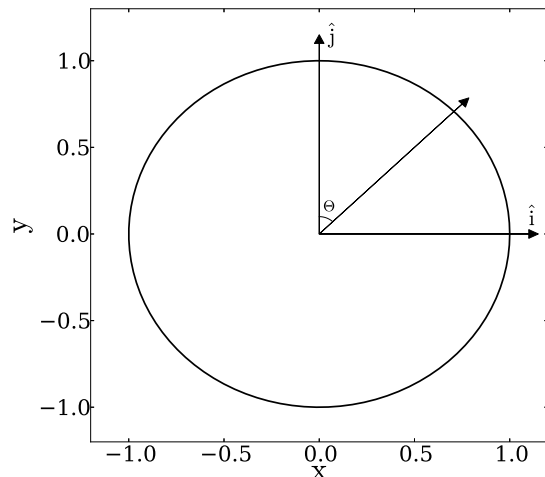


FIG. 1.— Geometry of the gas distribution. The angular velocity vector is parallel to the unit vector  $\hat{k}$ . In order to describe the departures from spherical symmetry we use the polar angle  $\theta$  formed by the direction of the outgoing photons with respect to the  $z$ -axis. We define the variable  $\mu \equiv \cos \theta$  to report to present our results.

this choice, the components of the gas bulk velocity field,  $\vec{v} = v_x \hat{i} + v_y \hat{j} + v_z \hat{k}$ , can be written as

$$v_x = -\frac{y}{R} V_{\text{max}}, \quad (1)$$

$$v_y = \frac{x}{R} V_{\text{max}}, \quad (2)$$

$$v_z = 0, \quad (3)$$

where  $R$  is the radius of the sphere and  $V_{\text{max}}$  is the linear velocity at the sphere's surface. The minus/plus sign in the  $x/y$ -component of the velocity indicates the direction of rotation. In this case we take the angular velocity in the same direction as the  $\hat{k}$  unit vector. With these definitions we can write the norm of the angular velocity as  $\omega = V_{\text{max}}/R$ .

For each photon in the simulation we have its initial position inside the sphere, direction of propagation  $\hat{k}_{\text{in}}$  and reduced frequency  $x_{\text{in}}$ . The photon's propagation stops once they cross the surface of the sphere. At this point we store the position, the outgoing direction of propagation  $\hat{k}_{\text{out}}$  and the reduced frequency  $x_{\text{out}}$ . We now define the angle  $\theta$  by  $\cos \theta = \hat{k}_{\text{out}} \cdot \hat{k} \equiv \mu$ , it is the angle of the outgoing photons with respect to the direction of the angular velocity. We use the variable  $\mu$  to study the anisotropy induced by rotation. Figure 1 shows the geometry of the problem and the important variables.

### 2.2. Brief Description of the Radiative Transfer Codes

Here we briefly describe the relevant points for the two radiative transfer codes we have used. For a detailed description we refer the reader to the original papers Forero-Romero et al. (2011); Dijkstra & Kramer (2012).

The codes follow the individual scatterings of Ly $\alpha$  photons as they travel through a 3D distribution of neutral Hydrogen. At each scattering the frequency of the photon (in the laboratory frame) and its direction of propagation change. This change in frequency is due to the

Physical Parameter (units)	Symbol	Values
Velocity ( $\text{km s}^{-1}$ )	$V_{\text{max}}$	0, 50, 100, 200, 300
Hydrogen Optical Depth	$\tau_H$	$10^5$ , $10^6$ , $10^7$
Dust Optical Depth	$\tau_a$	0,1
Photons Distributions		Central, Homogeneous

TABLE 1  
SUMMARY OF PHYSICAL PARAMETERS OF OUR MONTE CARLO SIMULATIONS.

peculiar velocities of the Hydrogen atom that absorbed and re-emitted the photon. If dust is present, the photon can interact either with a Hydrogen atom or dust grain. In the case of a dust interaction the photon can be either absorbed or scattered, this probability is encoded in the dust albedo,  $A$ , which we chose to be  $1/2$ . In order to obtain accurate values for the escape fraction of photons in the presence of dust, we do not use any accelerating mechanism in the radiative transfer. Once the photons escape the gas distribution we store their direction at their direction of propagation and frequency at their last scattering.

The photons are thus emitted in some region of the gas distribution and follow a random walk in space and frequency until they escape the gas distribution or are absorbed by a dust grain. The initialization process for the Ly $\alpha$  photons has to specify its position, frequency and direction of propagation. In our case we select the initial frequency to be exactly the Ly $\alpha$  rest-frame frequency ( $x = 0$ ) and the direction of propagation to be random following a flat probability distribution over the sphere. A different initialization that uses a Gaussian with a velocity with equal to the thermal velocity,  $12.8 \text{ km s}^{-1}$  in our case, should not introduce noticeable change given that our rotational velocities span the range  $100\text{-}300 \text{ km s}^{-1}$  and the lines have velocity widths on the order of  $100\text{-}500 \text{ km s}^{-1}$ .

The gas is completely defined by its geometry (i.e. sphere or slab), temperature  $T$ , Hydrogen optical depth  $\tau_H$ , dust optical depth  $\tau_a$  and the bulk velocity field  $\vec{v}$ . Our codes treat the gas as homogeneous in density ( $\tau_H$ ,  $\tau_a$ ) and temperature.

### 2.3. Grid of Simulated Galaxies

In the Monte Carlo calculations we follow the propagation of  $N_\gamma = 10^5$  numerical photons through different spherical galaxies. For each galaxy we vary at least one of the following parameters: the maximum rotational velocity  $V_{\text{max}}$ , the hydrogen optical depth  $\tau_H$ , the dust optical depth  $\tau_a$  and the initial distribution of photons with respect to the gas. There are 60 models initial combining all variations of the input parameters. Table 1 summarizes the different parameters.

Additionally, we have used two independently developed Monte Carlo codes (Forero-Romero et al. 2011; Dijkstra & Kramer 2012) to perform the calculations. The results we report are robust in the sense that they are obtained by both codes.

## 3. RESULTS

The central results of this paper are evident in Figures 2 and 3. They show 2D histograms of escape frequency  $x$  and escape angle  $\theta$  parameterized by  $|\mu|$  after verifying that the solutions are symmetric with respect to  $\mu = 0$ .

Making a selection around a given value of  $\mu$  gives us the line detected by an observer located at an angle  $\theta$  with respect to the rotation axis.

From these Figures we can see that the line properties change with rotational velocity and depend on the viewing angle  $\theta$ . In the next subsections we describe in detail the changes of the morphology with velocity, optical depth and viewing angle. We characterize the line morphology by its total intensity, the full width at half maximum (FWHM) and the location of the peak maxima. In order to interpret the morphological changes in the line we also report the median number of scatter for each Ly $\alpha$  photon in the simulation. For the models where dust is included we measure the escape fraction as a function of rotational velocity.

### 3.1. Line Morphology

The first column in both Figures 2 and 3 shows that for the static sphere the line properties are independent of  $|\mu|$ , as it is expected due to the spherical symmetry. However, for increasing rotational velocities, at a fixed optical depth, there are clear signs that this symmetry is broken.

If the viewing angle is aligned with the rotation axis,  $|\mu| \sim 1$ , the Ly $\alpha$  line keeps a double peak with some changes as a function of the rotational velocity that are easier to spot in models where the Ly $\alpha$  photons are homogeneously distributed than in the case of central emission.

However, for a line of sight perpendicular to the rotation axis,  $|\mu| \sim 0$ , the impact of rotation is larger. This is clear in Figure 4 where we present the different line morphologies for  $|\mu| \sim 0$  for both the homogeneous and central configurations. The panels have the same distribution as Figures 2 and 3.

There are three clear effects on the line's morphology as the rotational velocity increases. First, the line broadens; second, the double peaks reduce their intensity; and third, the intensity at the line center rises. The last two effects merge to give the impression that the double peaks are merged into one at high rotational velocities, a result that is evident for the homogeneously distributed sources as shown in the dashed lines of Figure 4.

In

### 3.2. Integrated Line Intensity

We consider possible variations in the integrated flux with respect to  $\theta$ .

We define the flux by:

$$F(\mu) = \frac{2\Delta N}{N\Delta\mu}, \quad (4)$$

Where  $\mu = \cos\Theta$ ,  $N$  is the total number of outgoing photons,  $\Delta N$  is the number of photons in an angular bin  $\Delta\Theta$ . This definition satisfies the condition  $\int_{-1}^1 F(\mu) d\mu / 2 = 1$ . With this definitions, the emission is characterized by a flat  $F(\mu)$  distribution as is shown in 5, this means that the amount of flux is the same for all of the angles.

We

### 3.3. Full Width at Half Maximum

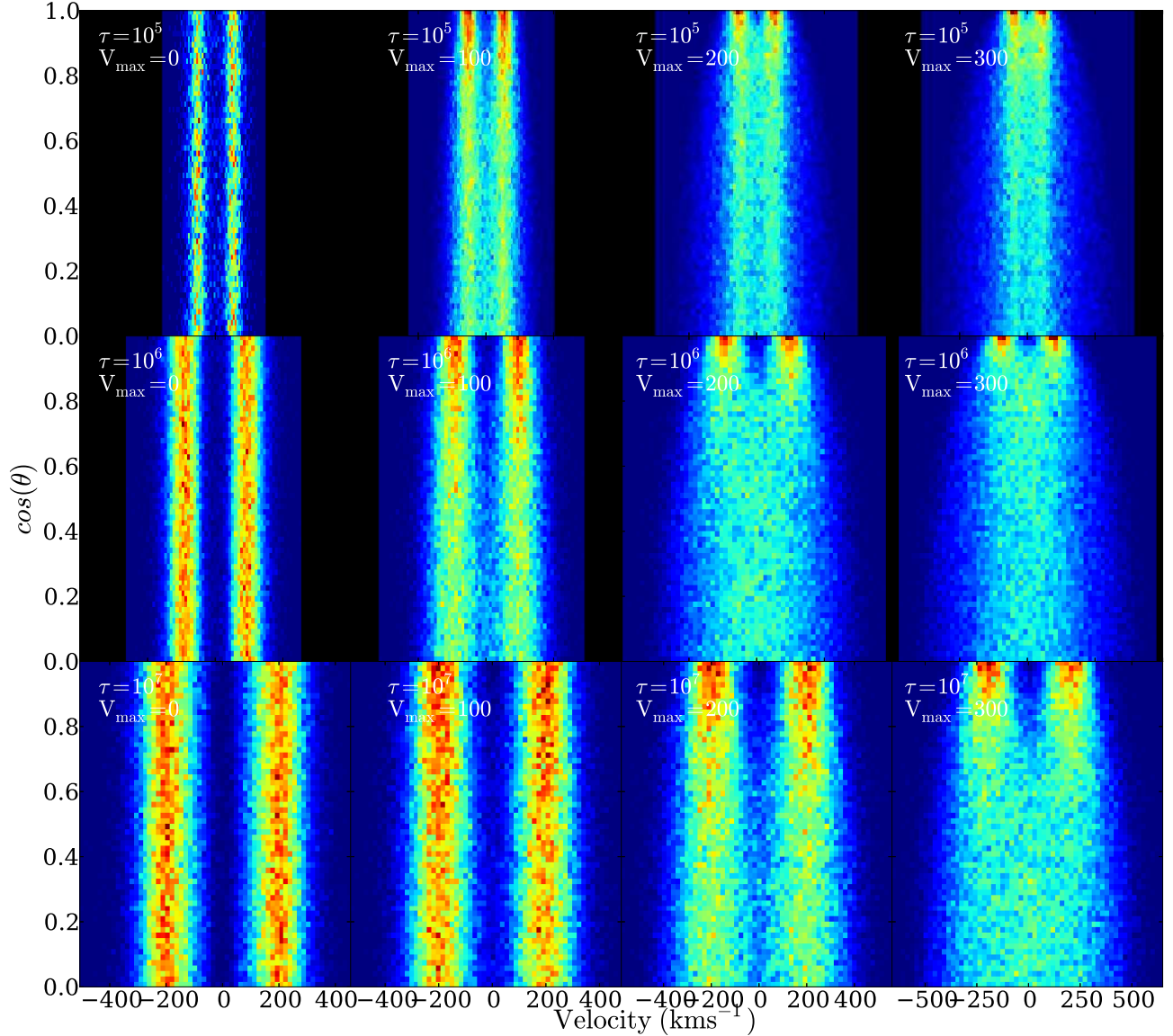


FIG. 2.— 2D histogram showing the number of photons that escape with frequency  $x$  forming an angle  $\theta$  (parameterized as  $\cos \theta$ ) with the rotation axis. The rotational velocity (0, 100, 200, 300 km s<sup>-1</sup>) increases from left to right and the optical depth ( $10^5$ ,  $10^6$ ,  $10^7$ ) from top to bottom. The Ly $\alpha$  photons are initialized at the center of the sphere.

We use the full width at half maximum (FWHM) to quantify the line broadening. For this we measure the width by interpolating dots in our spectra this would produce a continuous spectra which makes easier to find the half maximum in our histogram numerically, just finding the values of the width at the half maximum. In Figure 6 the effect of the viewing angle is shown, the main effects here are that as  $\mu$  increase the FWHM decrease this is also explained by the same argument of section XX. The second effect is that clearly as  $V_{\max}$  increase the FWHM also increase.

Figure ?? shows how the FWHM increases with rotational velocity both for the central (continuous lines) and homogeneous (dashed lines) sources, for  $\theta = \pi/2$ . We parametrize the dependency of the line width with  $V_{\max}$  as

$$\text{FWHM}^2 = \text{FWHM}_0^2 + V_{\max}^2/\lambda^2, \quad (5)$$

where  $\text{FWHM}_0$  is the velocity width in the static case and  $\lambda$  is a positive scalar to be determined as a fit to the data. With this test we want to know to what extent the new velocity width can be expressed as a quadratic sum of the two relevant velocities in the problem. We fit simultaneously all the points corresponding to central and homogeneous models to find  $\lambda_c = 3.89 \pm 0.04$  and  $\lambda_h = 1.98 \pm 0.06$  respectively.

### 3.4. Peaks Positions

In order to quantify the transition to a single peak we measure the position for the peak maxima as a function of the rotational velocity. Our results are presented in Figure 8 where it is clear that for central sources there are two peaks with fixed positions as the rotational velocity changes, with the only exception of the model with  $\tau_H = 10^6$  and  $V_{\max} = 300$  km s<sup>-1</sup>. However, in the case of homogeneously emitted sources the maxima position re-



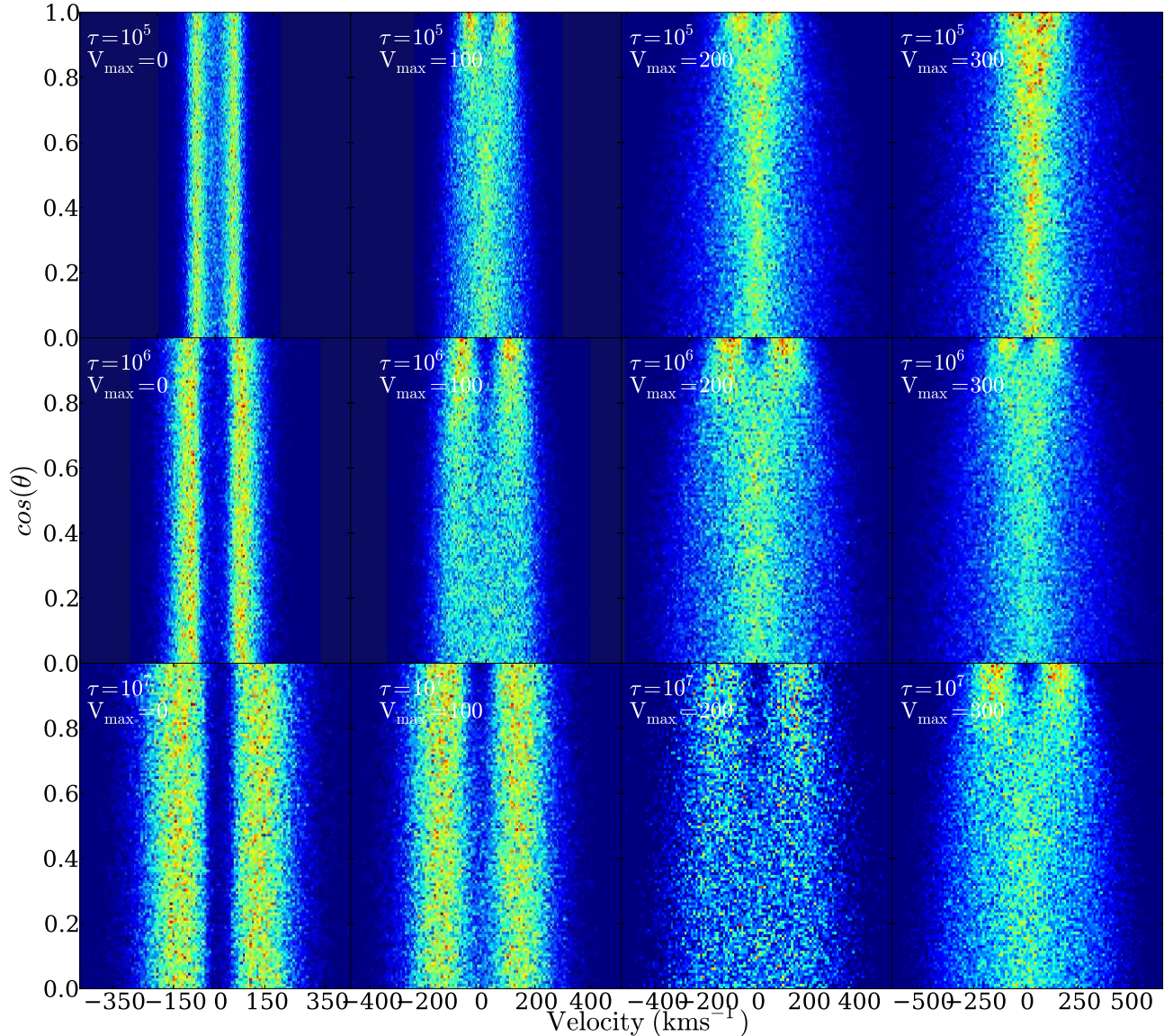


FIG. 3.— Same as Figure 2 for Ly $\alpha$  photons initialized homogeneously throughout the sphere.

main fixed until some velocity threshold is reached and the line becomes single peaked with  $x_m = 0$ . By inspection we find that in all cases the transition has occurred when the rotational velocity is larger than half the FWHM.

One possible explanation for the emergence of the single peak in the homogeneous systems is that some photons close to the surface (a sort of photosphere) can escape with a low number of scatterings, allowing them to stay close to the line's center. Increasing the rotational velocity  $V_{\max}$  reduces the optical depth making the photosphere region effectively larger, increasing the number of photons escaping close to the line's center.

However, for the central emission the transition to a single peak is almost never completed in the range of explored parameters. The absence of a single peak phase could be partially explained by the absence of a photosphere. In this case the average number of scatterings to escape should remain close to constant as the rotational velocity increases. The rise in intensity at the line's cen-

ter could instead mean that the scattering in a medium with bulk motion are inefficient in driving photons outside that frequency region.

In order to explore our interpretation for these two scenarios we now quantify the effect of rotation on the number of scatterings.

### 3.5. Dusty Clouds: Escape Fraction

In the case of dusty clouds, all changes in the average number of scatterings presented in the previous subsection have a direct bearing on the escape fraction. From the results we have just obtained we can predict that for central source distributions the escape fraction will barely change, while larger effects should be expected for homogeneously distributed sources.

Left panel of Figure 9 confirm these expectations. It shows the escape fraction as a function of the rotational velocity. The curves for the central source distribution stay flat, while for the homogeneous case there is a clear rise with rotational velocity. Rotation has a higher rel-

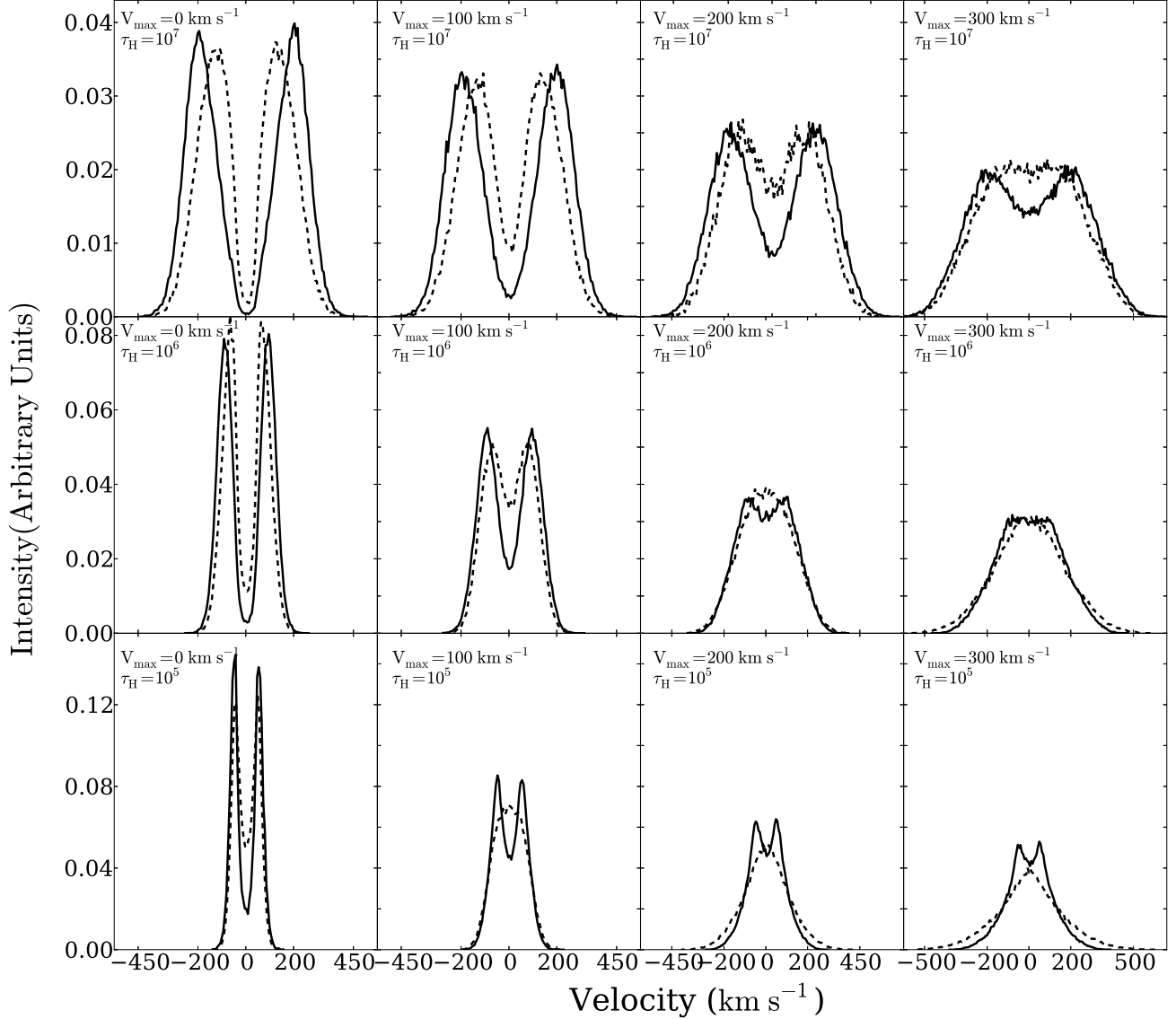


FIG. 4.— Shape of the Ly $\alpha$  line for different maximum rotational velocities for a viewing angle perpendicular to the rotation axis ( $|\mu| \sim 0$ ). The continuous (dashed) line represents the central (homogeneous) source distributions. The panels follow the same correspondence as Figures 2 and 3.

Source Distribution	$\tau_H$	$V_{\max}$ (km s $^{-1}$ )				
		0	50	100	200	300
Homogeneous	$10^5$	0.263	0.266	0.309	0.357	0.370
	$10^6$	0.289	0.289	0.309	0.360	0.393
	$10^7$	0.227	0.229	0.231	0.254	0.281
Central	$10^5$	0.096	0.097	0.096	0.096	0.096
	$10^6$	0.066	0.066	0.066	0.066	0.066
	$10^7$	0.015	0.016	0.016	0.016	0.015

TABLE 2  
ESCAPE FRACTION VALUES FOR ALL DUSTY MODELS.

active impact in the models with low optical depth. For instance, in models with  $\tau_H = 10^5$ , the static escape fraction is 0.26 and increases to 0.37 for  $V_{\max} = 300$  km s $^{-1}$ . Table 2 lists all the values for the escape fraction.

In the right panel of Figure 9 we put these results in the context of the analytic solution for the infinite slab

(Neufeld 1990). In Neufeld’s set-up the analytic solution depends uniquely on the product  $(a\tau_H)^{1/3}\tau_A$  where  $\tau_A = (1 - A)\tau_a$ , an approximation that is valid only in the limit  $a\tau_H \gg 1$ . The dashed lines in the right panel of Figure 9 show the results for the different rotational velocities for the homogeneous models. First of all we note that the escape fraction does not increase significantly from  $\tau_H = 10^5$  to  $\tau_H = 10^6$ . This counter-intuitive result is a consequence of the transition into the ‘extremely’ opaque regime, which occurs roughly when  $a\tau_H > 10^3$  e.g. (Neufeld 1990).

### 3.6. Average Number of Scatterings

The number of scatterings affects the escape frequency of a Ly $\alpha$  photon. In static cases, a large value of the optical depth correlates with a high number of scatterings, increasing the probability of finding a Ly $\alpha$  photon far from the line’s center. As a result the peak maxima shifts from the center as the amount of neutral hydro-

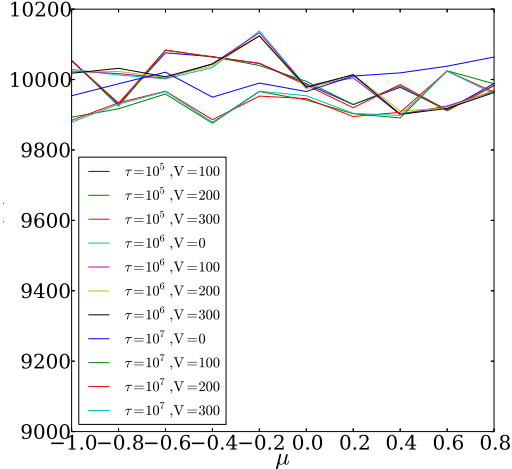


FIG. 5.— Integrated flux distribution,  $F(\mu)$ , as a function of the viewing angle as parameterized by  $\mu$ . We show the results for the homogeneous source distribution in models with rotational velocities 0, 100, 200, 300  $\text{km s}^{-1}$  and optical depths  $10^5$ ,  $10^6$ ,  $10^7$ . We see that the distribution is flat, meaning that the flux for all viewing angles is the same. The results for the central sources are similar.

gen increases. This can be precisely quantified in the static slab with central sources where the maxima position are related to the optical depth and the temperature as  $x_m = \pm 1.066(a\tau_H)^{1/3}$  (Harrington 1973). In the same model the average number of scatterings depends only on the optical depth  $\langle N_{\text{scatt}} \rangle = 1.612\tau_H$  (Adams 1972; Harrington 1973), in the case of homogeneously distributed sources  $\langle N_{\text{scatt}} \rangle = 1.16\tau_H$  (Harrington 1973).

In Figure 11 we show the average number of scatterings  $\langle N_{\text{scatt}} \rangle$  as a function of the rotational velocity  $V_{\text{max}}$ . For the central source distribution the average number of scatterings  $\langle N_{\text{scatt}} \rangle$  changes less than 0.5% for different velocities. In this set-up the number of scatterings is proportional to the optical depth, with  $\langle N_{\text{scatt}} \rangle = (1.50, 1.00, 0.92)\tau_H$  for optical depth values of  $\tau_H = (10^5, 10^6, 10^7)$  respectively.

In Figure 11 we can see the decrease of  $\langle N_{\text{scatt}} \rangle$  as  $V_{\text{max}}$  increases in the homogeneous source distribution. For instance, for  $\tau_H = 10^5$  the average number of scatterings decreases by 61% at  $V_{\text{max}} = 300 \text{ km s}^{-1}$  in comparison to the static case.

For the homogeneous static sphere we find that  $\langle N_{\text{scatt}} \rangle = (0.99, 0.59, 0.51)\tau_H$ , this represents factors of (0.66, 0.59, 0.55) lower than the centrally emitted photons. While for the homogeneous rotating sphere at  $V_{\text{max}} = 300 \text{ km s}^{-1}$  we find that  $\langle N_{\text{scatt}} \rangle = (0.38, 0.34, 0.42)\tau_H$  which represents factors of (0.26, 0.34, 0.46) lower than the corresponding central case.

In order to gain a deeper understanding of these results and explain the results for the maxima in the line morphology we make 2D histograms for the number of scatterings as a function of the outgoing dimensionless frequency  $x$ . In Figure 12 we show such histograms in the case  $\tau_H = 10^5$  for the static case and  $V_{\text{max}} = 300 \text{ km s}^{-1}$ . The upper (lower) panels show the results for the homo-

geneous (central) source distribution. The color scale is logarithmic in the number of photons at a certain value  $x - N_{\text{scatt}}$ .

The top right panel of Figure 12 (homogeneous sources, high rotational velocity) supports our hypothesis about the photo-sphere in the homogeneous distribution. In this case most of the photons that left with  $x \sim 0$  have escaped with less than 10 scatterings. This also explains the decrease in the average number of scatterings observed in Figure 11.

However, for a central distribution the situation is quite different (lower panels). In this case the number of scatterings remains high, in the order of the optical depth, but the two peaks do get closer to each other. Here the most probable physical picture is that each scattering, due to the bulk velocity of the gas, is inefficient in driving the photon outside the line center.

#### 4. DISCUSSION

Gas bulk rotation has a noticeable effect on the morphology of the Ly $\alpha$  line. In this section we discuss the implications of these findings for the interpretation of available observational data.

The presence of single peaked profiles has been associated to inflow/outflow dynamics (Verhamme et al. 2006; Dijkstra & Kramer 2012). In this paper we show that gas bulk rotation can also be considered as a probable origin for that behavior, provided that the observed single peak is highly symmetric. Similarly, in the case of double peaked lines with a high level of flux at the line center, rotation also deserves to be considered in the pool of possible bulk flows responsible for that feature, specially if the two peaks have similar intensities. The case of triple peaked lines is another clear feature of gas rotation under the additional condition of an off-centered emission.

#### 5. CONCLUSIONS

This paper quantifies for the first time in the literature the effects of rotation in the morphology of the Ly $\alpha$  emission line in star forming galaxies. The results are based on the study of an homogeneous sphere of gas with solid body rotation. We explore a range of models by varying the rotational speed, hydrogen optical depth, dust optical depth and initial distribution of Ly $\alpha$  photons with respect to the gas density. As a cross-validation, we obtain our results from two independently developed Monte-Carlo radiative transfer codes.

Our main result is that rotation clearly impacts the Ly $\alpha$  line morphology. Double peaked lines can make transitions into single peaked lines as the rotational velocity increases. In the case of off-centered emission we obtain triple peaked lines for certain values of optical depth and rotational velocities.

Quantitatively the main results of our study are summarized as follows.

- In spite of the asymmetry induced by rotation the spatial anisotropy in the emission is usually below the 10% level. This justifies our consideration of angle-averaged effects to quantify the emission line of rotating clouds.
- The line width increases with rotational velocity. The line width approximately follows the func-

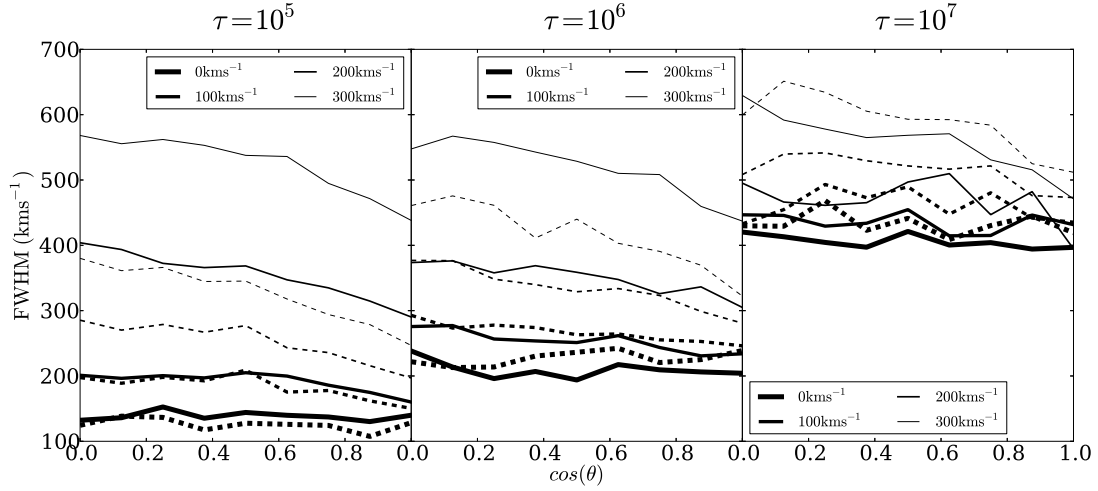


FIG. 6.— FWHM for the non-dusty models as a function of rotational velocity  $V_{\max}$ . The left panel shows the results in velocity units while the right panel normalizes the data by the FWHM in the static case. Continuous (dashed) lines correspond to central (homogeneous) source distributions. The straight lines represent the fit to the data using the expression in Eq. (5).

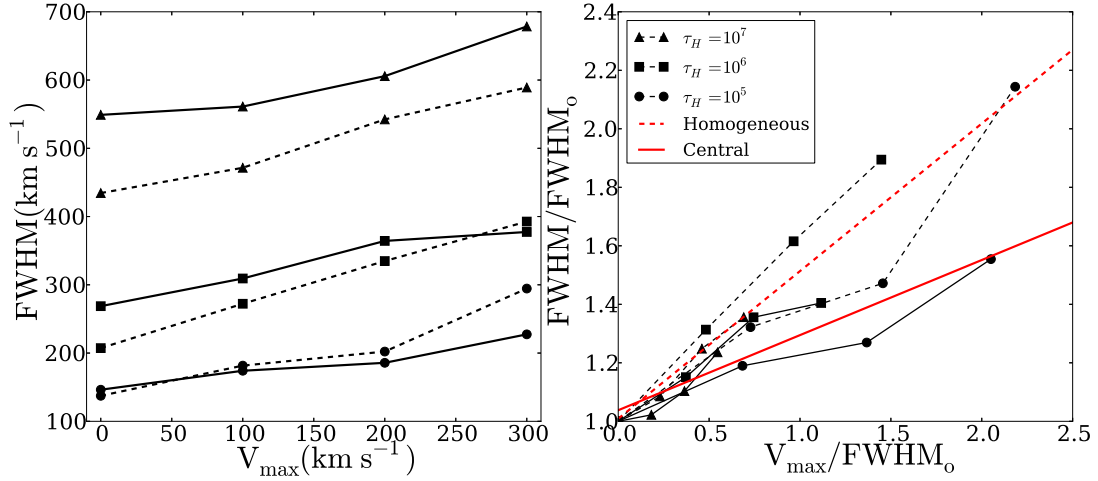


FIG. 7.— Position of the peak maxima as a function of rotational velocity  $V_{\max}$ . Continuous (dashed) lines correspond to central (homogeneous) source distributions. A value of  $x_{\max} = 0$  indicates that line becomes single peaked.

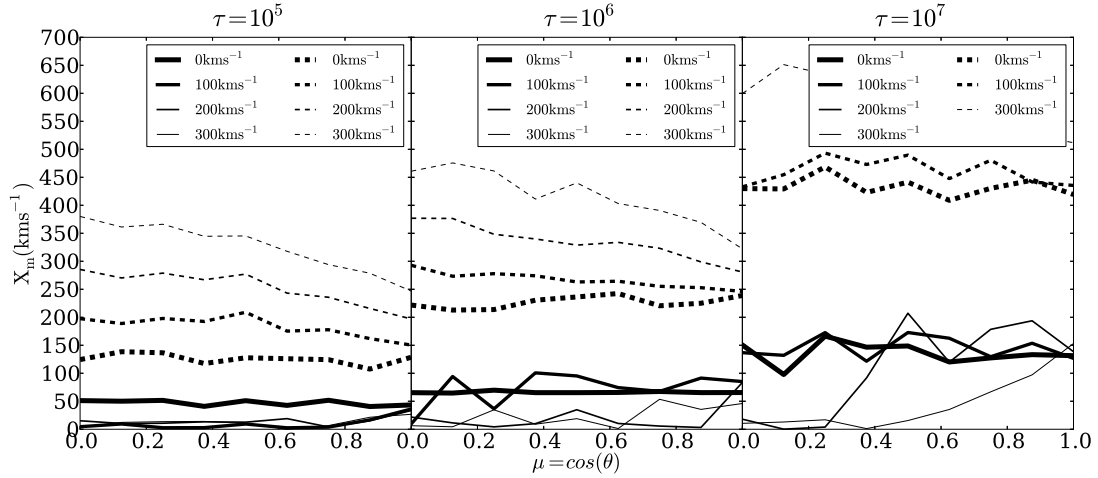


FIG. 8.— Position of the peak maxima as a function of rotational velocity  $V_{\max}$ . Continuous (dashed) lines correspond to central (homogeneous) source distributions. A value of  $x_{\max} = 0$  indicates that line becomes single peaked.



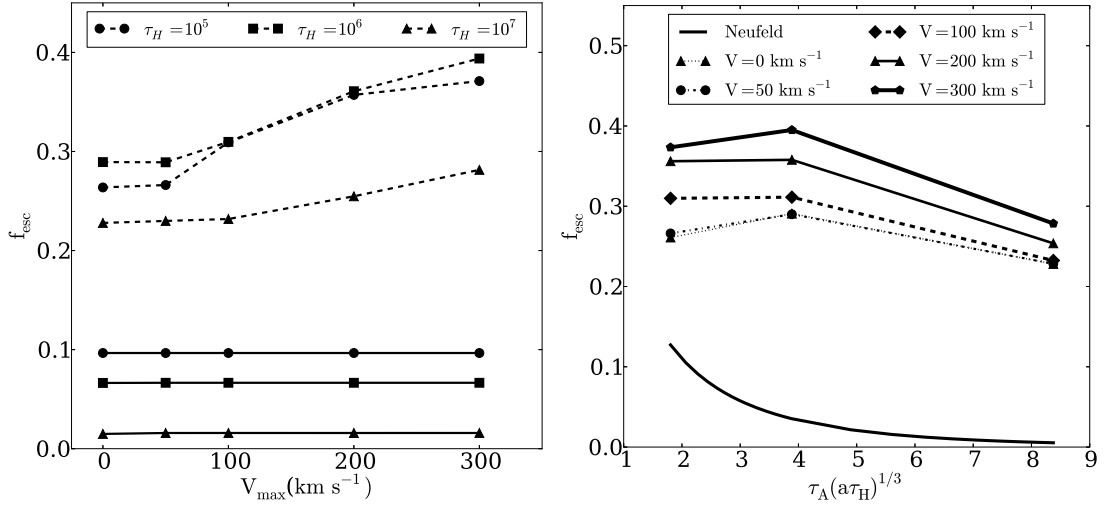


FIG. 9.— Effects of rotation on the escape fraction. Left panel, escape fraction as a function of rotational velocity. All these models have  $\tau_a = 1$ . The continuous (dashed) lines correspond to central (homogeneous) models. Right panel, escape fraction as a function of the product  $(a\tau_H)^{1/3}\tau_A$ . The analytic solution for the infinite slab is shown as a continuous line. Different lines correspond to different rotational velocities for the homogeneous models.

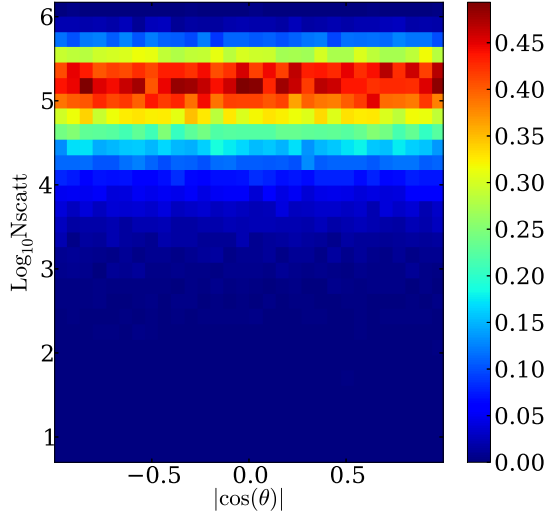


FIG. 10.— Logarithm of the average number of scatterings as function of  $\mu$ . This is the general behavior for all models in particular this model is for  $\tau = 10^5$  and  $V_{max} = 300 \text{ km/s}^{-1}$ .

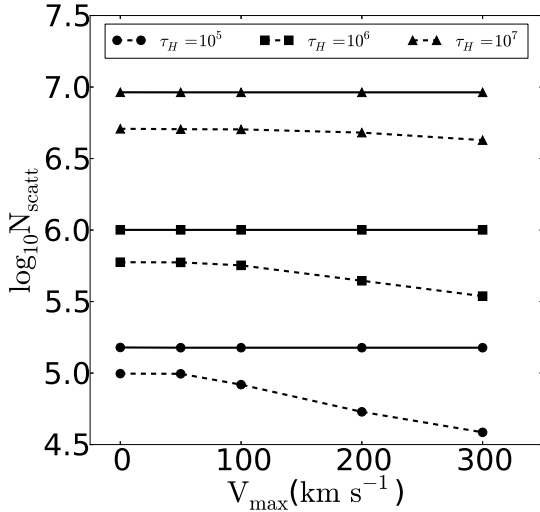


FIG. 11.— Logarithm of the average number of scatterings as function of rotational velocity. Continuous (dashed) lines represent an central (homogeneous) distribution of sources.

tional for  $\text{FWHM}^2 = \text{FWHM}_0^2 + (V_{max}/\lambda)^2$  where  $\text{FWHM}_0$  indicates the line width for the static case and  $\lambda$  is a constant determined from the radiative transfer results it is  $\lambda_c = 3.89 \pm 0.04$  and

$\lambda_h = 1.98 \pm 0.06$  for the central and homogeneous source distribution, respectively.

- A single peaked line emerges for high rotational velocities in the case of homogeneously distributed sources. These cases occur when the rotational velocity is larger than half  $\text{FWHM}_0$ .
- For central sources we find that the number of scatterings does not significantly decrease with rotation. This is due to the fact that the vast majority of scatterings events are resonant, during which the mean free path is very short and the effect of gas bulk rotation is not enough to affect Ly $\alpha$  photons. In consequence, the escape fraction neither the position of the peaks depends on the rotational velocity. However, there is a flux increase with rotational velocity in the central parts of the line.
- For homogeneous sources we find that the changes in the line morphology are linked to the reduction in the average number of scatterings. In the second part of §3.3 we show that, as rotational velocity increases, a large fraction of photons escape with less than 10 scatterings. The average number of scatterings decreases a 40% compared to the static case. This reduction in the number of scatterings decreases the probability for a photon to move away from the line's center. This is also translated into an increase of the escape fraction by a factor of  $\sim 2$  with respect to the static situation.

Comparing our results with recent observed LAEs we find that many morphological features such as high central line flux, single peak profiles could be explained by gas bulk rotation present in these LAEs.

#### ACKNOWLEDGMENTS

JNGC acknowledges financial support from Universidad de los Andes.

JEFR acknowledges financial support from Vicerrectoria de Investigaciones at Universidad de los Andes through a FAPA grant.

We thank the International Summer School on AstroComputing 2012 organized by the University of California High-Performance AstroComputing Center (UC-HiPACC) for providing computational resources where some of the calculations were done.

The data, source code and instructions to replicate the results of this paper can be found here <https://github.com/jngaravitoc/RotationLyAlpha>. Most of our code benefits from the work of the IPython and Matplotlib communities (Pérez & Granger 2007; Hunter 2007).

#### REFERENCES

- Adams, T. F. 1972, *ApJ*, 174, 439  
Ahn, S.-H., Lee, H.-W., & Lee, H. M. 2000, *Journal of Korean Astronomical Society*, 33, 29  
—. 2001, *ApJ*, 554, 604  
Ahn, S.-h., Lee, H.-w., & Lee, H. M. 2014, 000  
Auer, L. H. 1968, *ApJ*, 153, 783  
Avery, L. W., & House, L. L. 1968, *ApJ*, 152, 493  
Barnes, L. A., Haehnelt, M. G., Tescari, E., & Viel, M. 2011, *MNRAS*, 416, 1723  
Behrens, C., Dijkstra, M., & Niemeyer, J. C. 2014, *A&A*, 563, A77  
Behrens, C., & Niemeyer, J. 2013, *A&A*, 556, A5  
Dijkstra, M., Haiman, Z., & Spaans, M. 2006, *ApJ*, 649, 14  
Dijkstra, M., & Kramer, R. 2012, *MNRAS*, 424, 1672

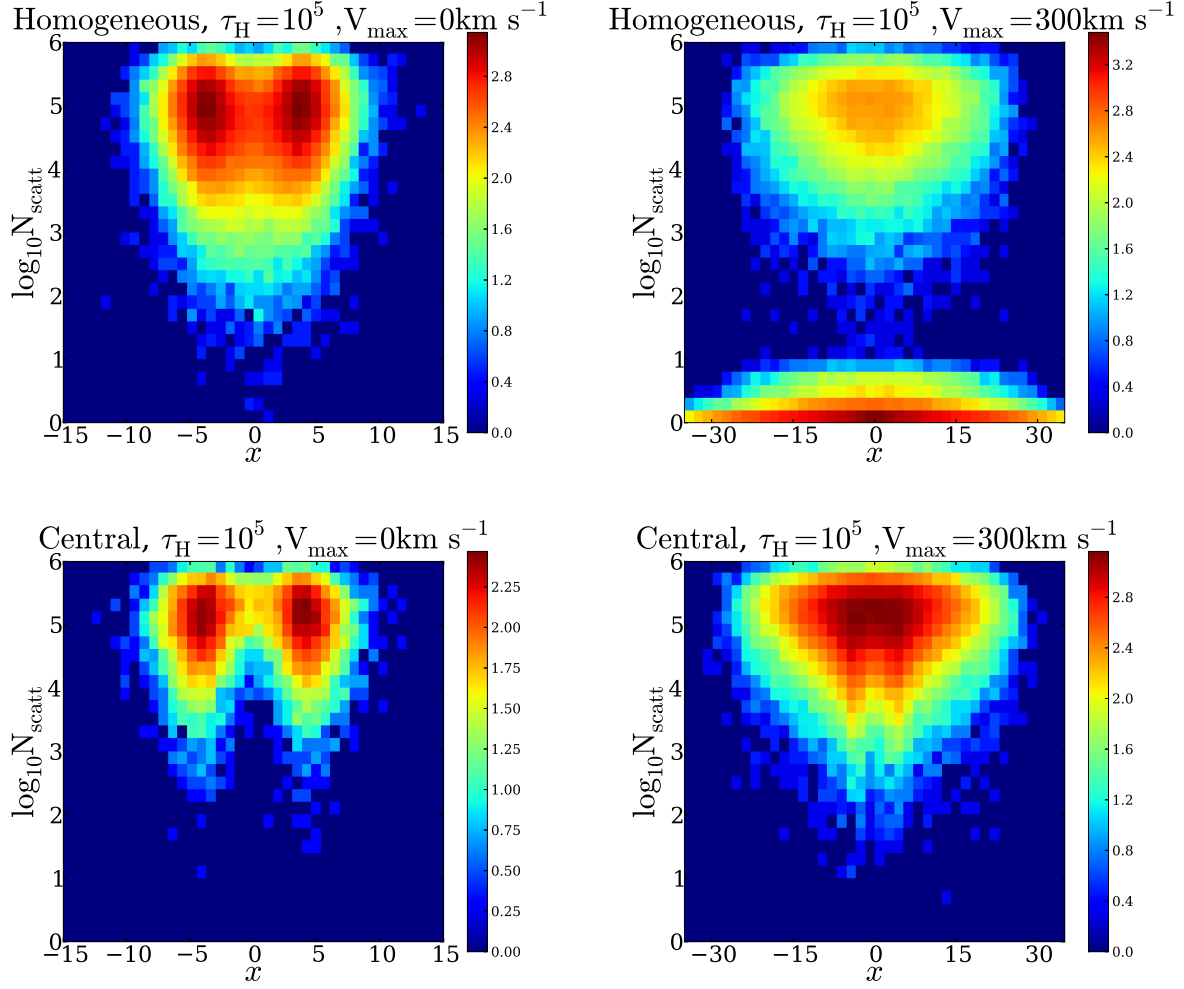


FIG. 12.— 2D histogram of  $N_{\text{scatt}}$  vs  $x$ . The upper (lower) panels show the homogeneous (central) source distribution. Left panels corresponds to the static case and right panels correspond to  $V_{\text{max}} = 300 \text{ km s}^{-1}$ . The color scale is logarithmic on the number of photons with given values of  $N_{\text{scatt}}$  and  $x$ .

Finkelstein, S. L., Papovich, C., Dickinson, M., Song, M., Tilvi, V., Koekemoer, a. M., Finkelstein, K. D., Mobasher, B., Ferguson, H. C., Giavalisco, M., Reddy, N., Ashby, M. L. N., Dekel, a., Fazio, G. G., Fontana, a., Grogin, N. a., Huang, J.-S., Kocevski, D., Rafelski, M., Weiner, B. J., & Willner, S. P. 2013, *Nature*, 502, 524  
Forero-Romero, J. E., Yepes, G., Gottlöber, S., Knollmann, S. R., Cuesta, A. J., & Prada, F. 2011, *MNRAS*, 415, 3666  
Forero-Romero, J. E., Yepes, G., Gottlöber, S., & Prada, F. 2012, *MNRAS*, 419, 952  
Garel, T., Blaizot, J., Guiderdoni, B., Schaerer, D., Verhamme, A., & Hayes, M. 2012, *MNRAS*, 422, 310  
Gawiser, E., Francke, H., Lai, K., Schawinski, K., Gronwall, C., Ciardullo, R., Quadri, R., Orsi, A., Barrientos, L. F., Blanc, G. A., Fazio, G., & Feldmeier, J. J. 2007, *ApJ*, 671, 278  
Hansen, M., & Oh, S. P. 2006, *MNRAS*, 367, 979  
Harrington, J. P. 1973, *MNRAS*, 162, 43  
Hunter, J. D. 2007, *Computing In Science & Engineering*, 9, 90  
Koehler, R. S., Schuecker, P., & Gebhardt, K. 2007, *A&A*, 462, 7  
Laursen, P., Sommer-Larsen, J., & Andersen, A. C. 2009, *ApJ*, 704, 1640  
Loeb, A., & Rybicki, G. B. 1999, *ApJ*, 524, 527  
Neufeld, D. A. 1990, *ApJ*, 350, 216

Orsi, A., Lacey, C. G., & Baugh, C. M. 2012, *MNRAS*, 425, 87  
Ouchi, M., Shimasaku, K., Akiyama, M., Simpson, C., Saito, T., Ueda, Y., Furusawa, H., Sekiguchi, K., Yamada, T., Kodama, T., Kashikawa, N., Okamura, S., Iye, M., Takata, T., Yoshida, M., & Yoshida, M. 2008, *ApJS*, 176, 301  
Partridge, R. B., & Peebles, P. J. E. 1967, *ApJ*, 147, 868  
Pérez, F., & Granger, B. E. 2007, *Computing in Science and Engineering*, 9, 21  
Rhoads, J. E., Malhotra, S., Dey, A., Stern, D., Spinrad, H., & Jannuzi, B. T. 2000, *ApJ*, 545, L85  
Schenker, M. A., Stark, D. P., Ellis, R. S., Robertson, B. E., Dunlop, J. S., McLure, R. J., Kneib, J.-P., & Richard, J. 2012, *ApJ*, 744, 179  
Verhamme, A., Dubois, Y., Blaizot, J., Garel, T., Bacon, R., Devriendt, J., Guiderdoni, B., & Slyz, A. 2012, *A&A*, 546, A111  
Verhamme, A., Schaerer, D., & Maselli, A. 2006, *A&A*, 460, 397  
Yajima, H., Li, Y., Zhu, Q., Abel, T., Gronwall, C., & Ciardullo, R. 2012, *ApJ*, 754, 118  
Yamada, T., Nakamura, Y., Matsuda, Y., Hayashino, T., Yamauchi, R., Morimoto, N., Kousai, K., & Umemura, M. 2012, *AJ*, 143, 79  
Zheng, Z., & Miralda-Escudé, J. 2002, *ApJ*, 578, 33  
Zheng, Z., & Wallace, J. 2013, *ArXiv e-prints*